ACS OMEGA

http://pubs.acs.org/journal/acsodf

Article

Snowflake-like Metastable Wurtzite $CuGaS_2/MoS_2$ Composite with Superior Electrochemical HER Activity

Jagan Radhakrishnan, Abdul Kareem, Srabanti Ratna, Sellappan Senthilkumar, and Krishnendu Biswas*

Cite This: *ACS Omega* 2022, 7, 43883−43893

Read Online

ACCESS | Metrics & More | Article Recommendations | Supporting Information

ABSTRACT: In the present work, we report the synthesis of wurtzite $CuGaS_2$ and its composite with MoS_2 and explored their efficacy toward two important applications, viz. electrocatalytic hydrogen evolution reaction (HER) and adsorption of Rhodamine B dye. The $CuGaS_2$ was synthesized via a low-temperature ethylenediamine-mediated solvothermal method. The obtained products were characterized by various techniques such as X-ray diffraction, field emission scanning electron microscopy, transmission electron microscopy, and X-ray photoelectron spectroscopy to ascertain the phase formation, surface morphology, and elemental oxidation states. The electrocatalytic activity of the wurtzite $CuGaS_2$ and $CuGaS_2/MoS_2$ composites toward HER was investigated, wherein the $CuGaS_2/MoS_2$ composite exhibited superior activity when compared to the pristine sample with a small Tafel slope of 56.2 mV dec^{-1} and an overpotential value of −464 mV at the current density of 10 mA cm^{-2}. On the other hand, the synthesized $CuGaS_2$ also showed an impressive adsorption behavior toward Rhodamine B dye with 99% adsorption in 60 min, which is relatively better than that observed with the composite material.

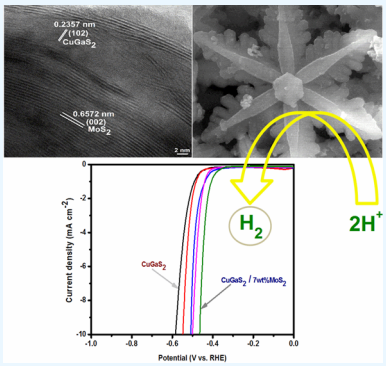

INTRODUCTION

In the past several decades, Pb- and Cd-based semiconductors which played a crucial role in various field of applications, viz. photocatalysis, light-emitting diodes, solar cells, etc., were limited for practical applications owing to their toxicity. This led to a surge in research for finding an alternative environmentally benign semiconductor material with reasonable efficiency compared to that of heavy-metal-based materials.[1−3] Recently, I−III−VI_2 ternary semiconductors have attracted much interest due to their narrow band gap, high stability against radiation, low cost, tunable emission wavelength, and high optical absorption coefficient.[4,5] Among the various Cu-based ternary chalcogenides, $CuGaS_2$ is greatly studied as a visible light photocatalyst, a light-emitting diode, and a host material in intermediate-band solar cells due to its low toxicity, good stability, and excellent electrical and optical properties. A direct band gap value of 2.4 eV makes it an efficient catalyst in the field of visible light photocatalyst applications.[6−8] Based on the arrangement of cations in the crystal lattice, it is known to exist in three polymorphic states, viz. thermodynamically stable tetragonal chalcopyrite, metastable hexagonal wurtzite, and cubic zinc blende phases.[9,10]

Generally, $CuGaS_2$ is synthesized by various methods like solid-state synthesis, spray pyrolysis, and chemical vapor deposition, which involve high temperatures, pressures, and special design of equipment.[11−14] In the present work, we chose the solvothermal method as it requires low temperatures and favors nanoparticles with the desired stoichiometry. Many reports on solvothermal synthesis of $CuGaS_2$ are found to generally yield the thermodynamically stable chalcopyrite phase, making the synthesis of the metastable wurtzite phase more challenging.[15−17] Only a few reports on wurtzite $CuGaS_2$ with various morphologies like tadpole structure for the photocatalytic degradation of Rhodamine B (RhB), nanosheets and nanorods for photoluminescent properties, and 2D nanoplates for enhanced photocatalytic hydrogen evolution exist. Hence tuning the property via a controlled phase and morphology is an important concern in the synthesis of these ternary chalcogenides.[18−20]

Over the past few decades, electrocatalytic water splitting has emerged as an ecofriendly and efficient method for hydrogen production. The huge cost of noble metals hinders their practical utilization, which has created a need to find alternative cost-effective electrocatalysts. In this regard, transition-metal-based materials including oxides, phosphides, carbides, chalcogenides, and nitrides have attracted great interest as potential candidates for the electrocatalytic hydrogen evolution reaction (HER).[21,22] Specifically, transition metal chalcogenides are found to be earth-abundant, rich in reactive sites, comprising specific structural properties and cost-effective catalysts for the HER.[23,24] Recently, some pioneering reports demonstrated that Cu-based sulfides such

Received: August 10, 2022
Accepted: October 28, 2022
Published: November 25, 2022

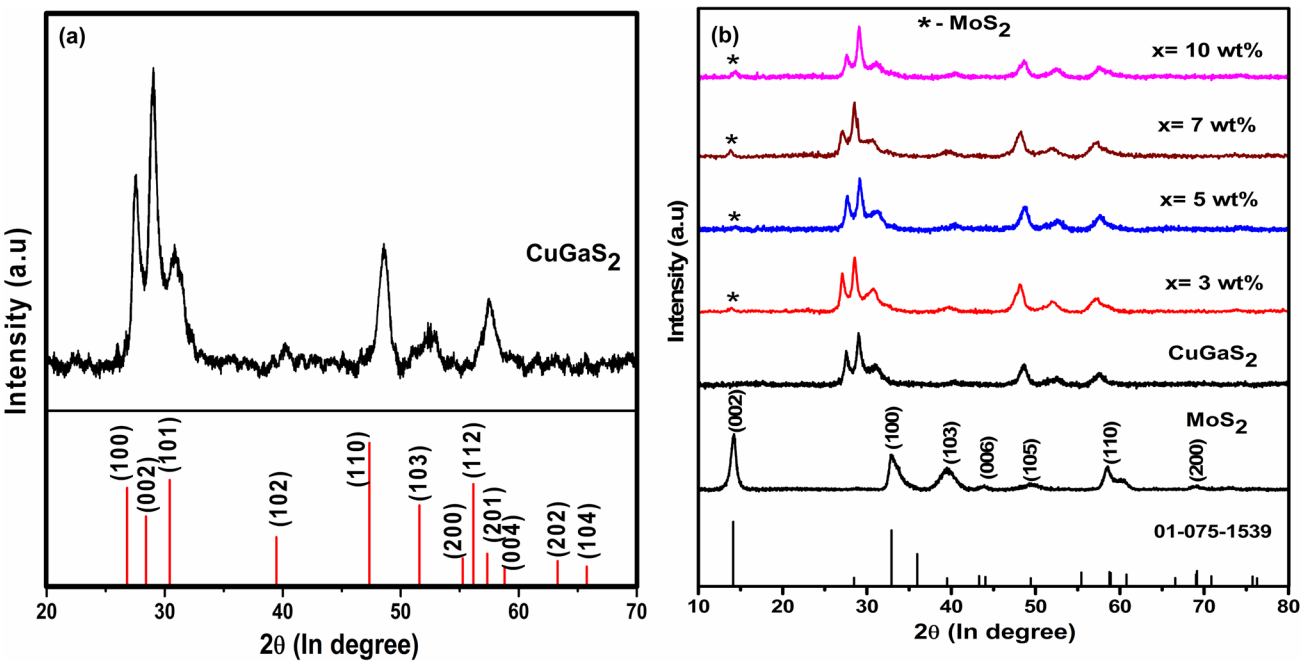

Figure 1. XRD patterns of the synthesized (a) wurtzite $CuGaS_2$ and (b) MoS_2, $CuGaS_2/xMoS_2$ composite (x = 0,3,5,7, 10 wt %).

as $CuFeS_2$, Cu_2SnS_3, Cu_2SnS_4, Cu_2WS_4, and Cu_2MoS_4 are efficient and stable electrocatalysts for the HER.[24−28] Similarly, $CuGaS_2$ and $CuInS_2$ are studied as promising photocathode materials for photoelectrochemical water splitting due to their superior electronic properties.[29,30] These studies reveal that $CuGaS_2$ could be explored as a suitable and interesting material for the electrocatalytic HER.

Furthermore, recent studies have demonstrated the enhancement of the catalytic activity of pure $CuGaS_2$ by the substitution of metal ions, coupling with noble metal, and construction of a heterostructure.[6,31−33] In addition to that described above, another way of enhancing the properties is by making composites, viz. $CuInS_2$/rGO or $CuInS_2$/g-C_3N_4, which showed efficient electrochemical behavior and adsorption properties.[34,35] The earth-abundant, stable, nontoxic 2D metal dichalcogenide MoS_2 is well-known to be a potential candidate in the field of photocatalysis, electrocatalysis, and environmentally related applications.[36−38] This motivated us to prepare pristine wurtzite $CuGaS_2$ and its composite with MoS_2 and evaluate their adsorption properties and electrochemical HER activity. We report a simple ethylenediamine-mediated solvothermal method for synthesizing wurtzite-phase $CuGaS_2$ and $CuGaS_2/MoS_2$ composites which were studied for Rhodamine B dye adsorption and electrochemical HER activity.

EXPERIMENTAL SECTION

$CuCl_2$ (SRL), Ga_2O_3 (Alfa Aesar), thiourea (SRL), concentrated HCl (Rankem), ethylenediamine (Loba), ethanol (Jiangsu Huaxi International), and Nafion (Sigma-Aldrich) were used as purchased.

First, 0.0375 g (0.2 mmol) of Ga_2O_3 was dissolved in a minimum quantity of concentrated HCl (0.2 mL) in mild heating conditions (60 °C). Then 0.0538 g (0.4 mmol) of $CuCl_2$ and excess thiourea (0.12 g) were taken in a 50 mL Teflon-lined autoclave to which 14 mL of ethylenediamine (EDA) was added and stirred for 10 min. Then the as-prepared $GaCl_3$ solution was added drop by drop to the above mixture, and the autoclave was sealed and placed in a hot air oven at a temperature of 150 °C for 15 h. For the preparation of the $CuGaS_2/MoS_2$ composites, MoS_2 was synthesized by the procedure reported in our previous work.[39] The corresponding $CuGaS_2/MoS_2$ weight ratio (3%, 5%, 7%, 10%) was calculated and added to the above mixture. After the autoclave was cooled to room temperature, the products were collected through centrifugation at 4500 rpm for 8 min. Then the precipitate was washed several times with distilled water and ethanol to remove the EDA. Finally, the obtained product was dried in a hot air oven at 80 °C for 8 h and used for further characterization.

Characterization. Powder X-ray diffraction analysis was performed to identify the phase formation of the synthesized composites using PANalytical X'Pert PRO with a scan rate of 5° per minute in the 2θ range from 10 to 80° (Cu Kα (λ = 0.15406 nm) radiation). Morphological and elemental analyses of the samples were carried out using field emission scanning electron microscopy (FESEM) (Zeiss) with energy-dispersive X-ray spectroscopy (EDAX). High-resolution transmission electron microscopy (HRTEM) (FEI-TECNAI G2-20 TWIN, JEOL Japan) was used for morphology studies. X-ray photoelectron spectroscopy (XPS) measurements were carried out using an ULVAC-PHI (PHI5000 Version Probe III) instrument to ascertain the valence state of the elements. All of the electrochemical studies were carried out with the help of an Autolab electrochemical workstation (PGSTAT204, Metrohom-Autolab, Netherlands; 2015). A UV−visible spectrometer (PerkinElmer Lambda 35) was used to study the Rhodamine B dye adsorption behavior of the synthesized catalysts.

Electrocatalytic HER Measurements. A conventional three-electrode system in 0.5 M H_2SO_4 was used to measure the electrochemical activity. The working electrode was prepared by coating the synthesized catalyst on the glassy carbon electrode (GCE). A graphite rod acted as the counter electrode and the Ag/AgCl electrode as the reference electrode. Initially, the GCE (surface area of 0.07 cm^2) was

https://doi.org/10.1021/acsomega.2c05116
ACS Omega 2022, 7, 43883−43893

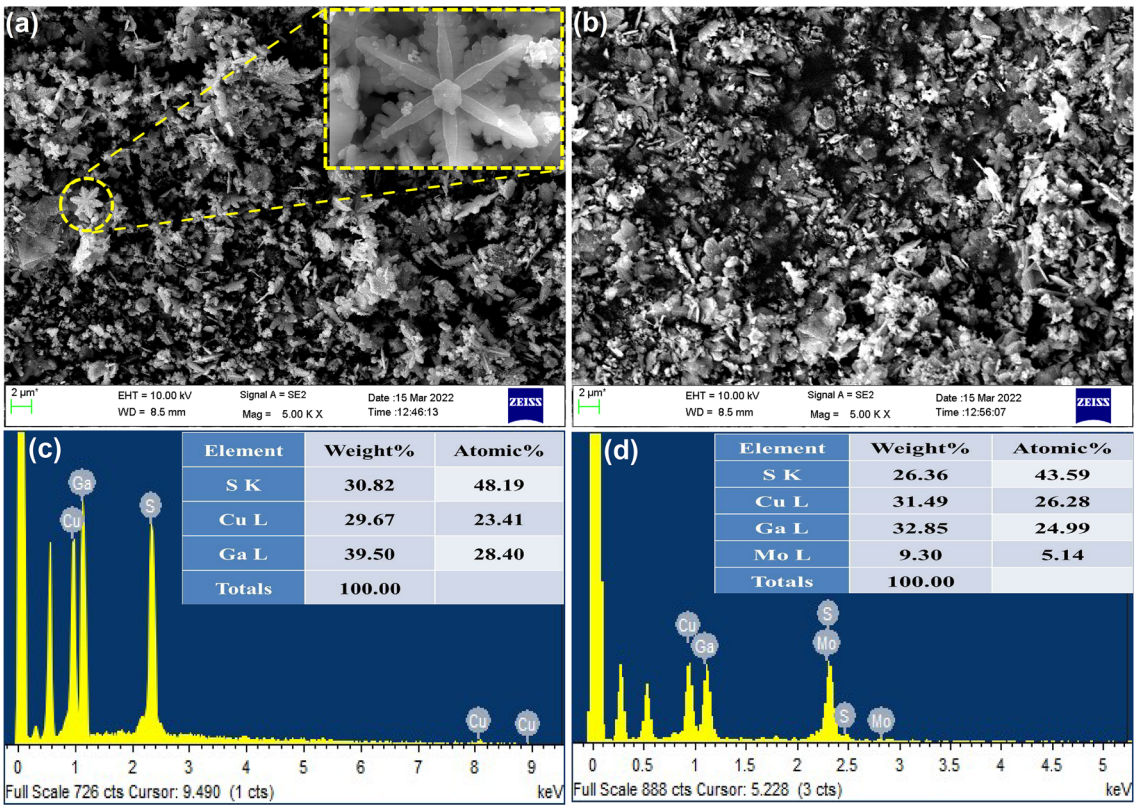

Figure 2. FESEM images (a,b) and EDAX spectra (c,d) of $CuGaS_2$ and $CuGaS_2$/7%MoS_2.

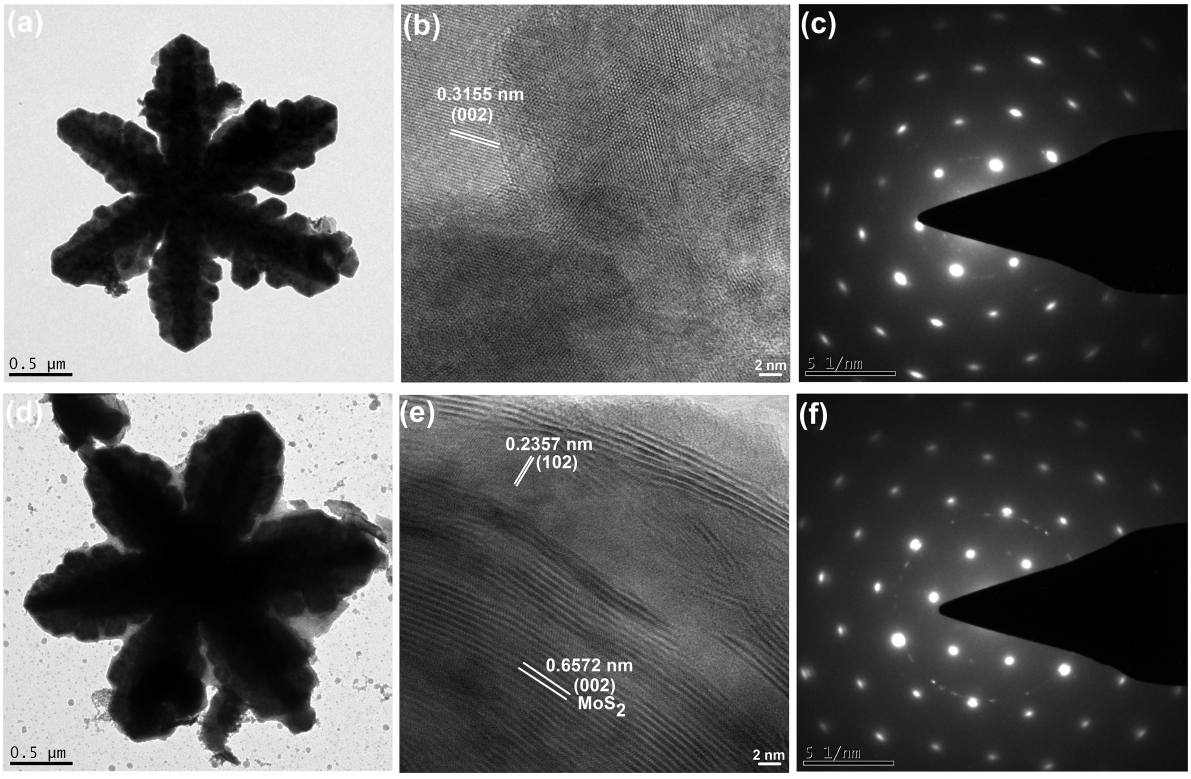

Figure 3. TEM images (a,d), HRTEM images (b,e), and SAED patterns (c,f) of $CuGaS_2$ and $CuGaS_2$/7%MoS_2.

polished with various alumina suspensions of 1 μm, 0.3 μm, and 50 nm, and the surface was cleaned with ethanol and distilled water. A homogeneous catalyst suspension (ink) was prepared by dispersing 5 mg of catalyst in a mixture of deionized water (250 μL), ethanol (245 μL), and 5 wt % Nafion (5 μL) and stirred. For better dispersion, the suspension was further ultrasonicated for 30 min at room temperature, and then the catalyst ink (3 μL) was drop-casted

https://doi.org/10.1021/acsomega.2c05116
ACS Omega 2022, 7, 43883−43893

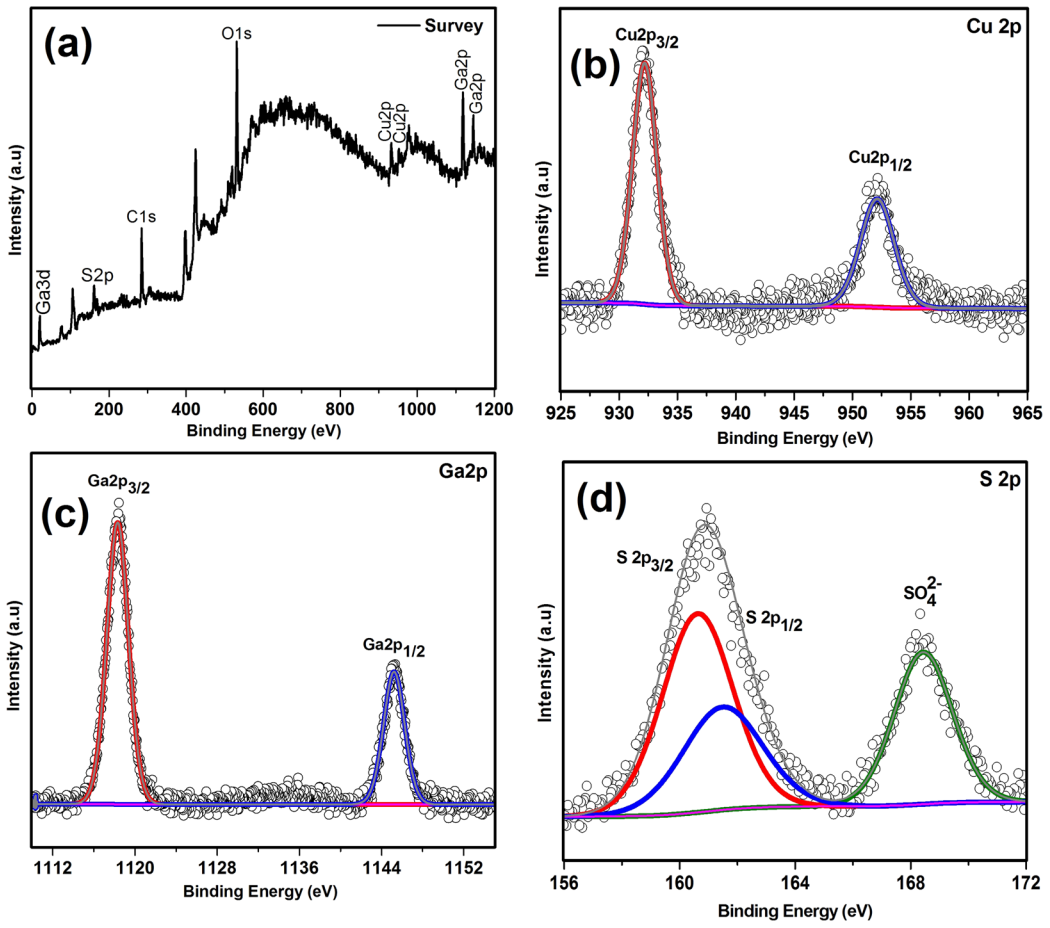

Figure 4. XPS spectra of $CuGaS_2$: (a) survey, (b) Cu 2p, (c) Ga 2p, and (d) S 2p.

on the GCE surface and dried at ambient temperature. Standardization of the referred potential versus the reversible hydrogen electrode (RHE) was calculated using the equation $E_{(RHE)} = E_{(Ag/AgCl)} + 0.059pH + 0.197$. The prepared catalysts are named as CGS, 3MCGS, 5MCGS, 7MCGS, and 10MCGS for $CuGaS_2$, $CuGaS_2$/3%MoS_2, $CuGaS_2$/5%MoS_2, $CuGaS_2$/7%MoS_2, and $CuGaS_2$/10%MoS_2, respectively.

RESULTS AND DISCUSSION

The XRD patterns of the synthesized compounds shown in Figure 1a reveal the formation of a single-phase wurtzite $CuGaS_2$ consistent with a previous report. The average crystallite size was found to be 15 nm, and the obtained lattice constants $a = b = 3.7406$ Å and $c = 6.1515$ Å matched with the reported values.[18,40] From the XRD patterns, it is evident that no peak for the chalcopyrite phase (JCPDS No. 00-025-0279) was observed, indicating that the synthesis method was able to stabilize a metastable wurtzite phase. The simulated XRD pattern of wurtzite $CuGaS_2$ corroborates our experimental pattern (crystal parameters are given in Table S1). The XRD pattern of $CuGaS_2$/MoS_2 composites given in Figure 1b matched the simulated wurtzite pattern along with the standard pattern of 2H MoS_2 (JCPDS No. 01-075-1539), confirming the successful formation of a composite without any additional phase.

The FESEM image (Figure 2a) of the synthesized wurtzite $CuGaS_2$ shows a snowflake-like structure which is further clearly visualized with the help of the FESEM image given in Figure 2a (inset), showing the growth of six petals on the six faces of the hexagon. The EDAX spectrum given in Figure 2c confirms the existence of all elements Cu, Ga, and S in the expected near stoichiometry. The FESEM image of the $CuGaS_2$/7%MoS_2 composite (Figure 2b) shows the presence of a snowflake-like structure, indicating the composite formation has not disturbed the parent morphology. FESEM images at different magnifications are given in Figure S1, which further confirms that the composite retains its morphology. According to Figure 2d, the EDAX spectrum confirms the presences of all elements Cu, Ga, Mo, and S in near stoichiometric composition of the composite material. The uniform distribution of the elements was confirmed by the density of dots from the elemental mapping (Figure S2).

The TEM image given in Figure 3a further confirms the snowflake structure of a few micrometers size with a lattice spacing of 0.3155 nm that is observed between two consecutive fringes in the HRTEM analysis (Figure 3b) corresponding to the (002) plane of wurtzite $CuGaS_2$.[20] The TEM image of the composite shows the snowflake-like morphology slightly covered with MoS_2 sheets, indicating that the composite construction does not affect the morphology of $CuGaS_2$. Figure S3 shows the TEM images at different magnifications, which further confirms the snowflake-like morphology of the synthesized compounds. The lattice spacing values of 0.2357 and 0.6572 nm in the HRTEM image of composite correspond to the (102) and (002) planes of wurtzite $CuGaS_2$ and MoS_2, respectively, confirming the successful formation of the composite.[20,41] The moderate bright spots observed in the selective area electron diffraction

https://doi.org/10.1021/acsomega.2c05116
ACS Omega 2022, 7, 43883−43893

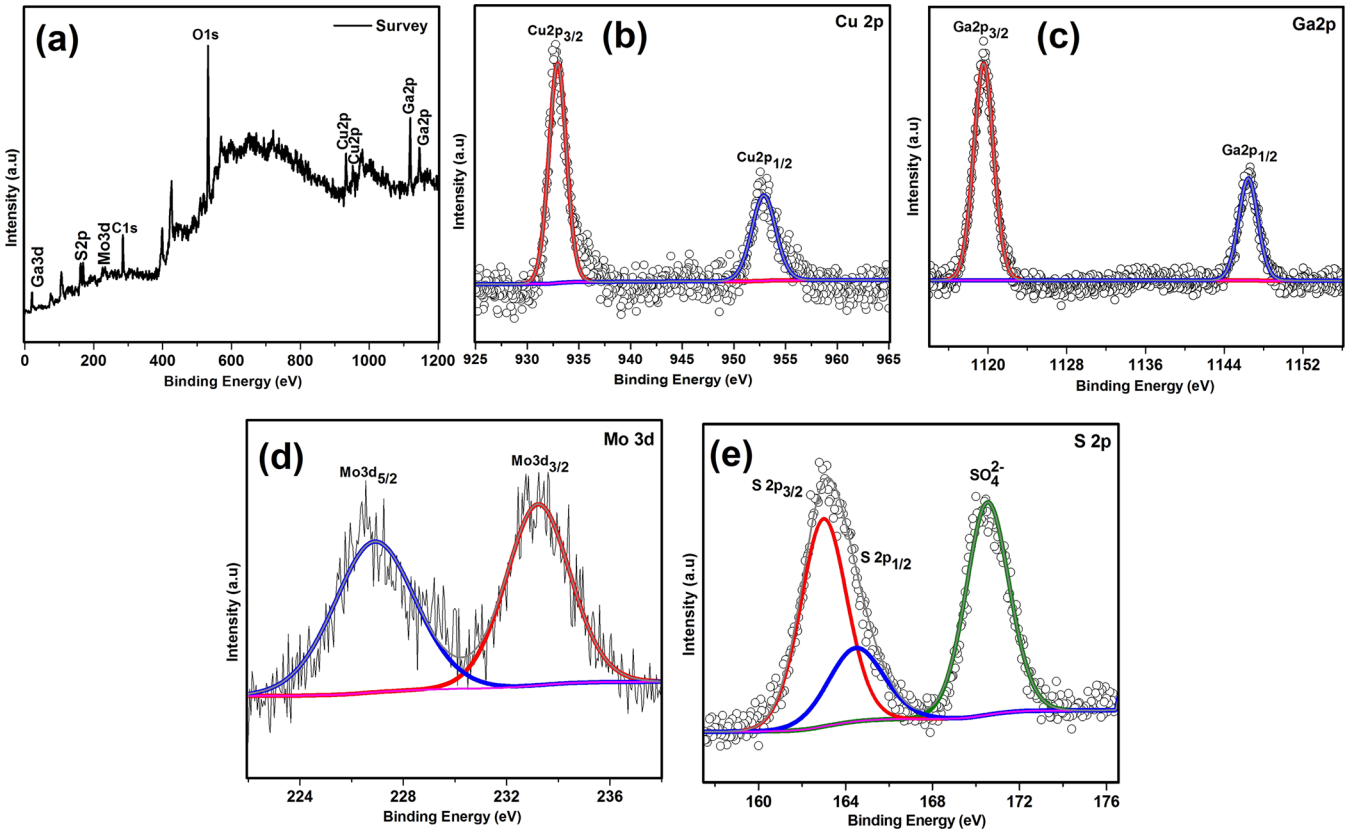

Figure 5. XPS spectra of $CuGaS_2$/7%MoS_2: (a) survey, (b) Cu 2p, (c) Ga 2p, (d) Mo 3d, and (e) S 2p.

(SAED) pattern of $CuGaS_2$ and the composite confirmed the polycrystalline nature of the synthesized compounds.

The XPS analysis survey spectrum of the synthesized compounds shown in Figure 4a confirms the presence of all three elements Cu, Ga, and S. The core level spectra of Cu 2p, Ga 2p, and S 2p are shown in Figure 4b–d, respectively. The peaks at the binding energy position of 932.41 eV ($2p_{3/2}$) and 952.24 eV ($2p_{1/2}$) in the core level spectrum of Cu with the peak separation of 19.83 eV confirm the +1 oxidation state of Cu.[42] The Ga 2p orbital spectrum shows the characteristic peaks of Ga^{3+} at the binding energy position of 1118.62 eV for $2p_{3/2}$ and 1145.49 eV for $2p_{1/2}$.[16] The peak position located at 161.2 eV in the core level spectrum of sulfur corresponds to S 2p, and the peak at 168.77 eV arises due to S–O bond.[16,43]

The survey spectrum of the synthesized composite ($CuGaS_2$/7%MoS_2) given in Figure 5a shows the existence of Mo, Cu, Ga, and S peaks, confirming the intact composition of the composite. The high-resolution XPS spectrum of Cu given in Figure 5b shows two peaks at the binding energy position of 932.65 and 952.8 eV, with the peak separation of 20.15 eV confirming the +1 oxidation state of Cu.[42] The two peaks at the binding energy positions of 1119.37 and 1146.33 eV observed in the high-resolution XPS spectra of Ga shown in Figure 5c correspond to Ga $2p_{3/2}$ and Ga $2p_{1/2}$, respectively.[16] The peaks at 226.9 and 233.2 eV in the high-resolution XPS spectrum of molybdenum given in Figure 5d confirm the +4 oxidation state of Mo.[44] The high-resolution XPS spectrum of S given in Figure 5e shows the characteristic peak at the binding energy position of 162.04 eV ascribed to S^{2-}, and the additional peak at the binding energy position of 169.14 eV is attributed to the S–O bond which is formed due to slight surface oxidation upon exposure to air.[24,43]

The electrochemical catalytic HER performances of the synthesized catalyst CGS, 3MCGS, 5MCGS, 7MCGS, and 10MCGS were analyzed in 0.5 M H_2SO_4 electrolyte using a typical three-electrode system. The HER activity of the prepared catalyst was measured by analyzing the linear sweep voltammetry (LSV), Tafel slope, and chronoamperometric technique. The linear sweep voltammetry curves of all samples shown in Figure 6a reveal an enhanced overpotential (η_{10}) value of −464 mV for the 7MCGS composite compared to other samples (Table 1) (*iR* corrected LSV curves are shown in Figure S4). The composites exhibited better activity than the bare $CuGaS_2$ due to the synergistic effect of $CuGaS_2$/MoS_2 composites, facilitating a rapid electron transfer.[45] The possible HER mechanistic pathway and performance of the catalyst were studied with the help of Tafel analysis. The Tafel slope was derived by fitting the linear portion of the Tafel plot using the Tafel equation ($\eta = b \log j + a$), where η is overpotential, b is the Tafel slope, and j is the current density. In general, the HER activity in acidic medium involved three possible mechanistic pathways as mentioned in the following eqs 1, 2, and 3 with the Tafel slope value of 120 mV/dec, 40 mV/dec, and 30 mV/dec, respectively.

$$H^+ + e^- + * \rightarrow H^* \text{ (Volmer reaction; * denotes an absorption site)} \quad (1)$$

$$H^* + H^+ + e^- \rightarrow H_2 \text{ (Heyrovsky reaction)} \quad (2)$$

$$H^* + H^* \rightarrow H_2 \text{ (Tafel reaction)} \quad (3)$$

From Table 1, the lowest Tafel slope value of 56.2 mV/dec is obtained for the 7MCGS composite, suggesting the

https://doi.org/10.1021/acsomega.2c05116
ACS Omega 2022, 7, 43883−43893

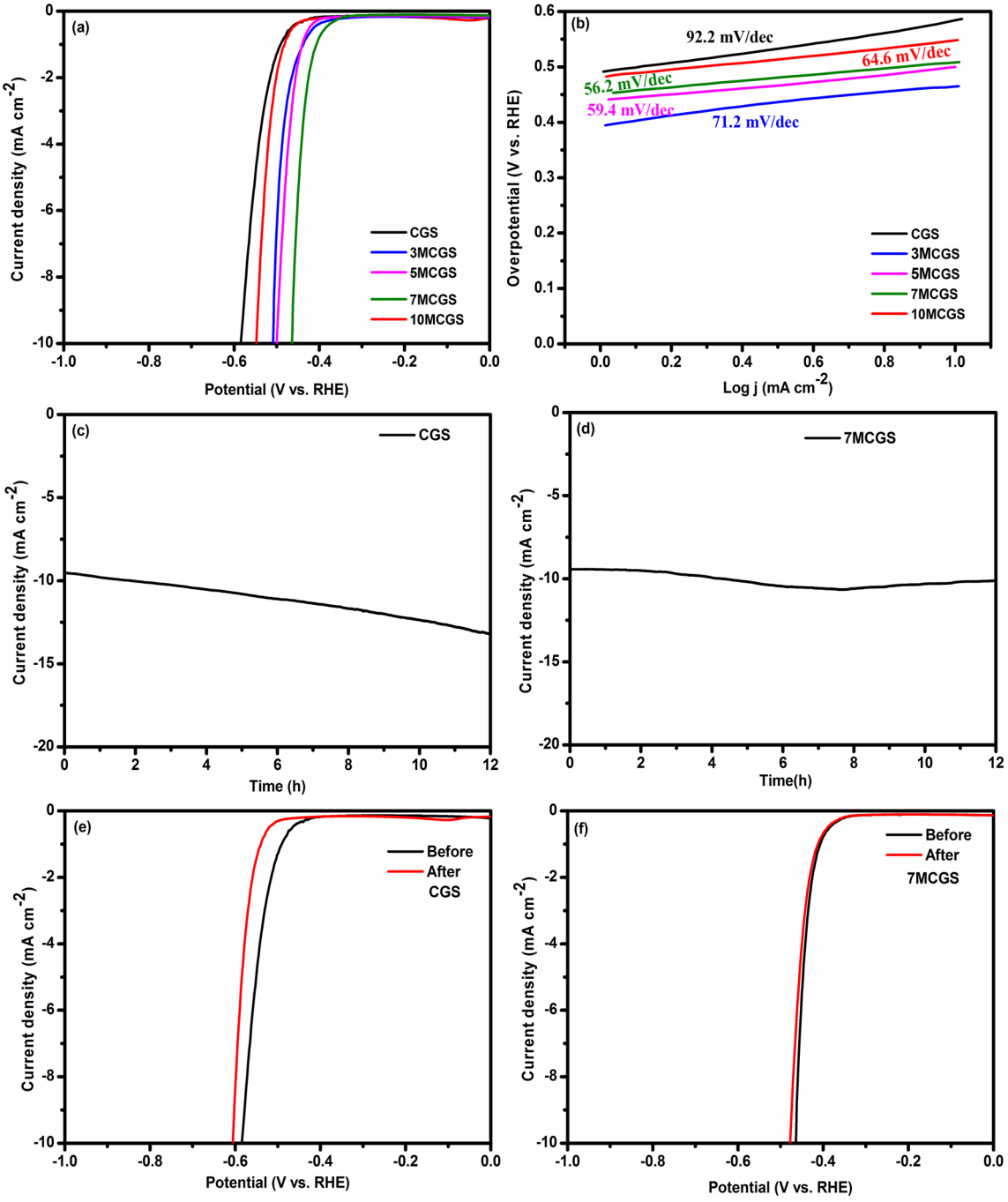

Figure 6. (a) Polarization curves of CGS, 3MCGS, 5MCGS, 7MCGS, and 10MCGS at a scan rate of 2 mV s^{-1}. (b) Tafel plot of CGS, 3MCGS, 5MCGS, 7MCGS, and 10MCGS in 0.5 M H_2SO_4. (c,d) Time-dependent current density curve for CGS and 7MCGS under static overpotential for 12 h and (e,f) LSV before and after chronoamperometric constant current electrolysis for CGS and 7MCGS.

Table 1. Electrochemical Parameters for Prepared Catalysts

catalyst	overpotential at 10 mACm^{-2} (mV)	Tafel slope (mV dec^{-1})	C_{dl} (mF)	ECSA (cm^2)
CGS	−583	92.2	0.533	13.32
3MCGS	−509	71.2	0.705	17.62
5MCGS	−499	59.4	0.888	22.20
7MCGS	−464	56.2	0.955	23.87
10MCGS	−547	64.6	0.678	16.95

improved kinetics of HER compared to that of other catalysts. Further, the low Tafel slope value suggests that the HER follows the Volmer−Heyrovsky mechanism, and the Heyrovsky step is the rate-determining step.[46−48] Another important parameter to understand the catalytic performance is electrochemical active surface area (ECSA) which is evaluated from the electrochemical double layer capacitance (C_{dl}) owing to their direct relation. The double layer capacitance value was measured from the non-faradaic potential region of the CV curves at different scan rates (50 mV s^{-1} to 10 mV s^{-1}), which are shown in Figure S5a,c,e,g,i. The linear fit of the current density with the scan rate shown in Figure S5b,d,f,h,j and the calculated double layer capacitance values given in Table 1 indicate an increase in the electrochemical active surface area for the composites.[49]

https://doi.org/10.1021/acsomega.2c05116
ACS Omega 2022, 7, 43883−43893

Among all of the samples, the 7MCGS composite showed the highest C_{dl} and ECSA values of 0.955 mF and 23.87 cm^2, respectively. These results clearly indicate that 7MCGS has more active sites facilitating the enhanced activity of the catalyst compared to other composites and the pristine compound. The consolidated HER parameters for the prepared catalysts are given in Table 1. The ECSA normalized LSV shown in Figure S6 reveals that the 7MCGS catalyst still has activity superior to that of the bare $CuGaS_2$ and remaining compositions, which again confirms that the intrinsic activity of $CuGaS_2$ is enhanced by the 7%MoS_2 composite construction.[50] Another intrinsic activity parameter, turn over frequency (TOF), of the catalysts was calculated, and the values are given in the Table S2 which shows that the 7MCGS has enhanced HER activity compared to that of the parent $CuGaS_2$ and all other composite compounds, which is attributed to increased intrinsic activity of the each active site.[51] Furthermore, the stability of the catalysts which is the main concern in the electrocatalytic HER reaction is ascertained by the chronoamperometric curve of the CGS and 7MCGS given in Figure 6c,d. It is evident from the curves that both catalysts exhibit excellent stability over the time period of 12 h with a slightly better stability for the composite. Both catalysts exhibited reliable stability which is also confirmed from the negligible overpotential difference observed in the obtained LSV curves of before and after stability tests for CGS and 7MCGS as given in Figure 6e,f. Further a small hysteresis in overpotential of 7MCGS compared to that of CGS confirms that the incorporation of MoS_2 with $CuGaS_2$ not only enhanced the overpotential but also provided admirable long-term durability. After the chronoamperometry stability test, the catalyst was characterized again using XRD and FESEM analysis. Figure S7a shows the XRD pattern of the electrocatalyst after the stability test, which exhibited diffraction peaks similar to those of the synthesized $CuGaS_2$/7%MoS_2, with relatively more noise. Further, the FESEM image (Figure S7b,c) shows that there was no significant change in the morphology even after electrolysis for 12 h. These studies ensure the long-term stability of the composite even after 12 h of electrolysis.

The electrochemical impedance spectroscopy (EIS) was carried out to support the improved HER activity of the 7MCGS electrocatalyst. As shown in Figure 7, the charge-transfer resistance (R_{ct}) of 7MCGS (245 Ω) is much lower than that of CGS (2763 Ω), suggesting rapid electrode kinetics and higher charge-transfer rate of 7MCGS.[52,53] Further, the electrocatalytic HER activity of the synthesized $CuGaS_2$/MoS_2 is compared in Table 2 with Cu- and Ga-based metal sulfides. Based on the obtained overpotential and Tafel slope values, it can be inferred that the $CuGaS_2$/MoS_2 composite exhibited better or comparable HER activity.

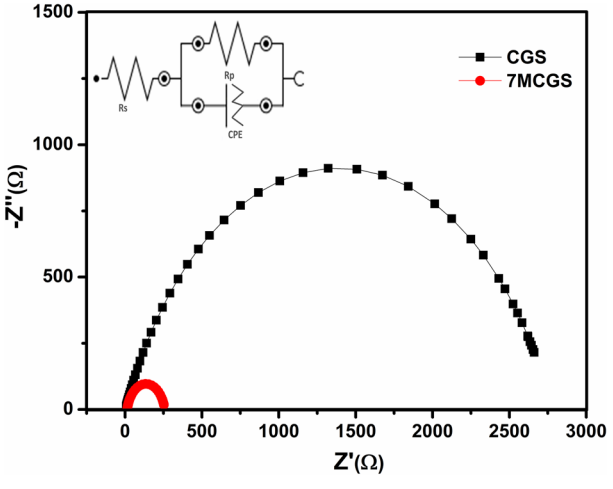

Figure 7. EIS curves of CGS and 7MCGS in 0.5 M H_2SO_4.

Recently, metal-sulfide-based semiconductor nanomaterials are extensively viewed as an adsorbent material for dye molecules for environmental remediation,[39,61−63] and we have explored the dye adsorption property of the synthesized $CuGaS_2$/$xMoS_2$ (x = 0, 5, 10 wt %) samples using Rhodamine B dye. The adsorption experiments were carried out in the dark and at room temperature. At first, 30 mg of $CuGaS_2$ samples was added into 50 mL of the RhB solution with an initial concentration of 10 ppm to confirm the adsorption capability. Four milliliters of the suspension was then taken out at certain time intervals (0−60 min) and taken for UV−visible spectroscopy measurements. The concentration of RhB was measured from the absorbance at 554 nm. Figure 8a shows the temporal evolution of the absorption spectrum of RhB dye solution in the presence of the $CuGaS_2$ catalyst. The considerable decrease in the intensity of the major absorption peak of the RhB molecule indicates the adsorption of RhB molecule taking place on $CuGaS_2$. It is clearly seen that around 90% of the RhB molecules are quickly adsorbed within 20 min, nearing completion in 60 min, which is attributed to the availability of more active sites. Figure 8d shows the removal % of dye as a function of contact time using the $CuGaS_2$ catalyst. The rapid adsorption of dye molecules on the catalyst may be attributed to the active S^{2-} sites at the surface of the $CuGaS_2$.[38] The quick adsorption behavior of the synthesized wurtzite $CuGaS_2$ can be utilized as a potential adsorbent for the removal of organic dye. The composite $CuGaS_2$/$xMoS_2$ (x = 5, 10 wt %) (Figure 8b,c) shows an adsorption activity inferior to that of $CuGaS_2$ which may be attributed to the coverage of active sites by the aggregated MoS_2 sheets.[64]

To the best of our knowledge, there are no reports available for the dye adsorption on $CuGaS_2$ and hence the adsorption behavior of the synthesized snowflake wurtzite $CuGaS_2$ is compared with the previously reported sulfide-based adsorbent materials (Table S3). To investigate the stability, the catalyst ($CuGaS_2$, $CuGaS_2$/5%MoS_2) after the adsorption process was washed several times with ethanol, centrifuged, and dried at 80 °C in a hot air oven. The recovered $CuGaS_2$ and $CuGaS_2$/5% MoS_2 were subjected to XRD analysis, and the obtained spectra are shown in Figures S8a and S9, respectively. It is clear from the XRD spectrum that the crystalline phase remains unchanged after the adsorption process. The morphology of the recovered $CuGaS_2$ catalyst was studied by FESEM analysis (Figure S8b), wherein no significant change in morphology was observed. These results confirm the excellent stability of the catalyst during the Rhodamine B dye adsorption process.

CONCLUSIONS

The metastable wurtzite phase of $CuGaS_2$ was synthesized by a solvothermal method at low temperature using ethylenediamine, followed by the preparation of $CuGaS_2$/MoS_2 composites. The 7MCGS composite showed an enhanced HER activity compared to that of the other composites and the pristine $CuGaS_2$, which is attributed to the increased electrochemical active surface area which in turn provides

https://doi.org/10.1021/acsomega.2c05116
ACS Omega 2022, 7, 43883−43893

Table 2. Comparative Analysis of Electrocatalytic HER Activity of Previously Reported Cu-, Ga-, and Mo-Based Metal Sulfide Electrocatalysts

S no.	sample	synthesis method	overpotential (η^{10}) (mV)	Tafel slope (mV dec^{-1})	ref
1	GaS nanosheets	liquid exfoliation	−570	85	54
2	CuS nanoplates	wet-chemical route/photoreduction	−449	171	55
3	$CuFeS_2$	colloidal chemistry method	−88.7	47	25
4	Cu_2WS_4	solvothermal	−650	121	27
5	Cu_2MoS_4	solution-processing method	−333	130.3	28
6	$Cu_2MoS_4/MoSe_2$ nanostructures		−166	74.7	
7	Cu_2SnS_3	solvothermal	−330	98	26
8	Cu_2SnS_4		−358	110	
9	Cu_2ZnSnS_4	hydrothermal	∼−1200	52	56
10	$NiCuCoS_3$-modified GE	solid-state method	−600	116.2	57
11	MoS_2	quartz glass tube K_2CO_3 + S + $MoO_3$750 °C/8 h	−610	∼200	58
12	$Mo_{0.93}Sn_{0.07}S_2$	solid vapor reaction 700 °C for 6 h	−403	170	59
13	MoS_2/NiO/MWCNT	MWCNTs +nickel oxide NPs + few-layered MoS_2 nanosheets/ magnetic stirring for 50 h		289	60
14	**$CuGaS_2$/7 wt %MoS_2 composite**	**solvothermal**	**−464**	**56.2**	**present work**

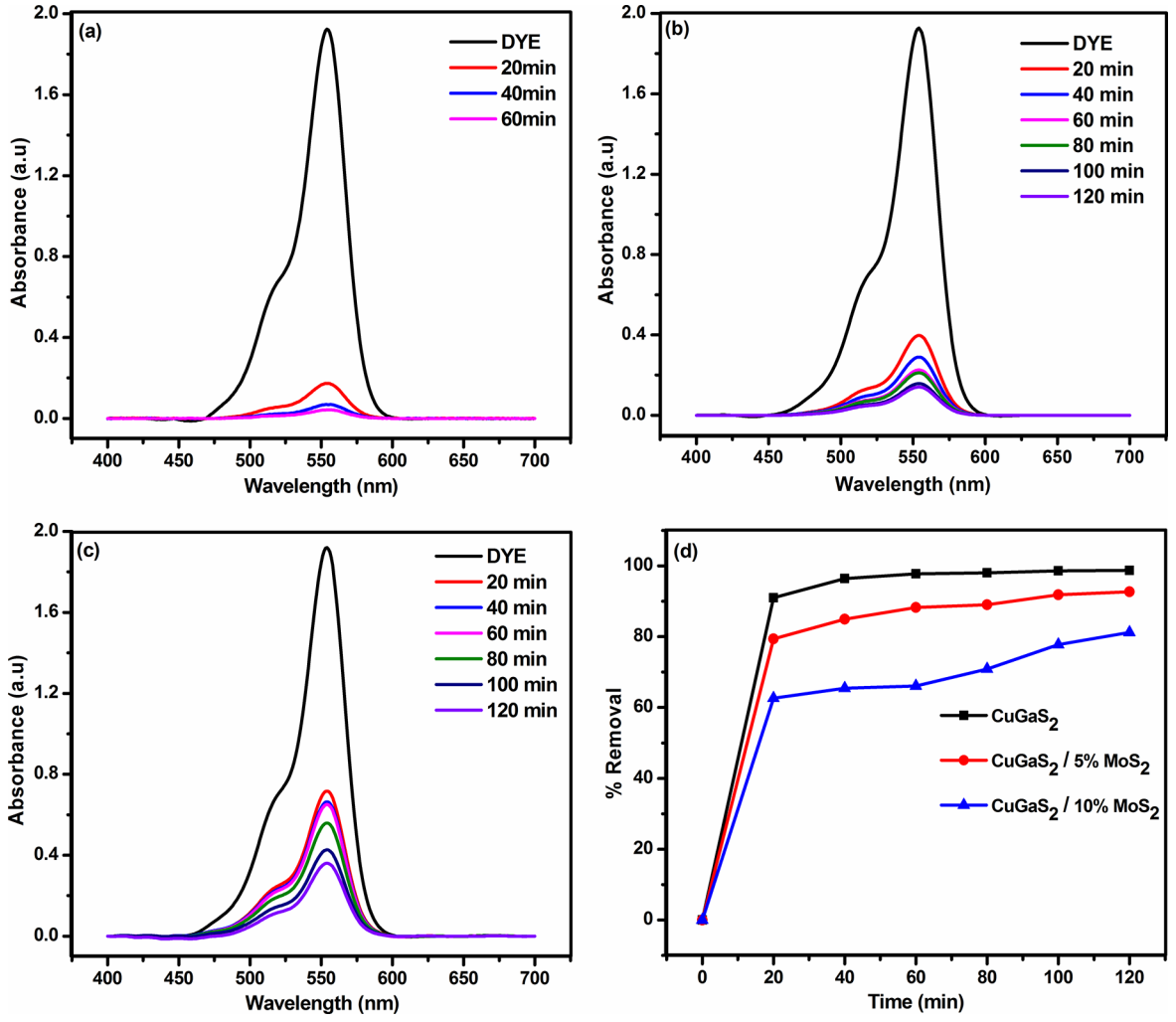

Figure 8. UV−visible absorption spectra for RhB (10 ppm) on (a) $CuGaS_2$, (b) $CuGaS_2$/5%MoS_2, and (c) $CuGaS_2$/10%MoS_2 catalysts and (d) removal efficiency of catalysts as a function of time.

more reactive sites. The catalyst 7MCGS exhibited a small Tafel slope value of 56.2 mV dec^{-1} with an overpotential value of −464 mV and a good stability for 12 h, making it a potential catalyst for HER activity. Further, the pristine wurtzite $CuGaS_2$ was found to be a good adsorbent for RhB dye with an almost complete removal achieved within 60 min.

https://doi.org/10.1021/acsomega.2c05116
ACS Omega 2022, 7, 43883−43893

■ ASSOCIATED CONTENT

Supporting Information

The Supporting Information is available free of charge at https://pubs.acs.org/doi/10.1021/acsomega.2c05116.

Crystal parameters of wurtzite $CuGaS_2$; FESEM images of $CuGaS_2$/7%MoS_2 in different magnifications; elemental mapping images of the $CuGaS_2$/7%MoS_2 composite; TEM image of $CuGaS_2$ and $CuGaS_2$/7% MoS_2 in different magnifications; *iR*-corrected LSV curves of CGS, 3MCGS, 5MCGS, 7MCGS, and 10MCGS for HER in 0.5 M H_2SO_4; CV curves at a non-faradic area in 0.5 M H_2SO_4 at scan rates of 10, 20, 30, 40, and 50 mV s^{-1} and capacitive currents plotted as a function of the scan rate of the CGS, 3MCGS, 5MCGS, 7MCGS, and 10MCGS electrodes; LSV curves of CGS, 3MCGS, 5MCGS, 7MCGS, and 10MCGS normalized by calculated ECSA; calculated TOF of catalysts; comparison for RhB adsorption performance of different sulfide based adsorbents; XRD patterns before and after HER activity and FESEM after HER activity of 7MCGS; XRD patterns before and after RhB adsorption, FESEM image, and EDAX after RhB adsorption of $CuGaS_2$; XRD patterns before and after RhB adsorption of $CuGaS_2$/5%MoS_2 (PDF)

■ AUTHOR INFORMATION

Corresponding Author

Krishnendu Biswas − *Chemistry Division, School of Advanced Sciences, Vellore Institute of Technology, Chennai 600127, India;* orcid.org/0000-0002-5476-7616; Email: krishnendu.biswas@vit.ac.in

Authors

Jagan Radhakrishnan − *Chemistry Division, School of Advanced Sciences, Vellore Institute of Technology, Chennai 600127, India*

Abdul Kareem − *Department of Chemistry, School of Advanced Sciences, Vellore Institute of Technology, Vellore 632014, India*

Srabanti Ratna − *Chemistry Division, School of Advanced Sciences, Vellore Institute of Technology, Chennai 600127, India*

Sellappan Senthilkumar − *Department of Chemistry, School of Advanced Sciences, Vellore Institute of Technology, Vellore 632014, India;* orcid.org/0000-0002-1770-2442

Complete contact information is available at: https://pubs.acs.org/10.1021/acsomega.2c05116

Notes

The authors declare no competing financial interest.

■ ACKNOWLEDGMENTS

The authors sincerely thank the VIT management for providing seed grant and all required support to carry out this research work.

■ REFERENCES

(1) Li, L.; Lou, Z.; Shen, G. Hierarchical CdS nanowires based rigid and flexible photodetectors with ultrahigh sensitivity. *ACS Appl. Mater. Interfaces* **2015**, *7*, 23507−23514.

(2) Safrani, T.; Kumar, T. A.; Klebanov, M.; Arad-Vosk, N.; Beach, R.; Sa'Ar, A.; Abdulhalim, I.; Sarusi, G.; Golan, Y. Chemically deposited PbS thin film photo-conducting layers for optically addressed spatial light modulators. *J. Mater. Chem. C* **2014**, *2*, 9132−9140.

(3) Kim, H.-J.; Lee, H.-D.; Pavan Kumar, C. S. S.; Rao, S. S.; Chung, S.-H.; Punnoose, D. The effect of manganese in a CdS/PbS colloidal quantum dot sensitized TiO_2 solar cell to enhance its efficiency. *New J. Chem.* **2015**, *39*, 4805−4813.

(4) Regulacio, M. D.; Han, M. Y. Multinary I-III-VI_2 and I_2-II-IV-VI_4 semiconductor nanostructures for photocatalytic applications. *Acc. Chem. Res.* **2016**, *49*, 511−519.

(5) Sangaré, K.; Cherfouh, H.; Marsan, B. Synthesis and Characterization of N-Type $CuGaS_2$ Nanoparticles and Films for Purpose of Photoelectrocatalytic Water Splitting. *J. Electrochem. Soc.* **2021**, *168*, 086506.

(6) Zhao, M.; Huang, F.; Lin, H.; Zhou, J.; Xu, J.; Wu, Q.; Wang, Y. $CuGaS_2$−ZnS p−n nanoheterostructures: a promising visible light photo-catalyst for water-splitting hydrogen production. *Nanoscale* **2016**, *8*, 16670−16676.

(7) Jo, D. Y.; Yang, H. Synthesis of highly white-fluorescent Cu−Ga−S quantum dots for solid-state lighting devices. *Chem. Commun.* **2016**, *52*, 709−712.

(8) Yang, C.; Qin, M.; Wang, Y.; Wan, D.; Huang, F.; Lin, J. Observation of an intermediate band in Sn-doped chalcopyrites with wide-spectrum solar response. *Sci. Rep.* **2013**, *3*, 1286.

(9) Abrahams, S. C.; Bernstein, J. L. Piezoelectric nonlinear optic $CuGaS_2$ and $CuInS_2$ crystal structure: Sublattice distortion in $A^IB^{III}C_2^{VI}$ and $A^{II}B^{IV}C_2^{V}$ type chalcopyrites. *J. Chem. Phys.* **1973**, *59*, 5415−5422.

(10) Wang, Y. H. A.; Zhang, X.; Bao, N.; Lin, B.; Gupta, A. Synthesis of shape-controlled monodisperse wurtzite $CuIn_xGa_{1-x}S_2$ semiconductor nanocrystals with tunable band gap. *J. Am. Chem. Soc.* **2011**, *133*, 11072−11075.

(11) Yamamoto, N.; Yokota, K.; Horinaka, H. Solid state growth of some I-III-VI_2 chalcopyrite crystals. *J. Cryst. Growth* **1990**, *99*, 747−751.

(12) Shirakata, S.; Saiki, K.; Isomura, S. Excitonic photoluminescence in $CuGaS_2$ crystals. *J. Appl. Phys.* **1990**, *68*, 291−297.

(13) Thirumalaisamy, L.; Ahsan, N.; Sivaperuman, K.; Kim, M.; Kunjithapatham, S.; Okada, Y. Engineering of sub-band in $CuGaS_2$ thin films via Mo doping by chemical spray pyrolysis route. *Thin Solid Films* **2020**, *709*, 138252.

(14) Sugan, S.; Baskar, K.; Dhanasekaran, R. Structural, optical and thermal properties of $CuGaS_2$ crystals by chemical vapor transport (CVT) method. *Optik* **2015**, *126*, 4326−4329.

(15) Lu, Q.; Hu, J.; Tang, K.; Qian, Y.; Zhou, G.; Liu, X. Synthesis of nanocrystalline $CuMS_2$ (M= In or Ga) through a solvothermal process. *Inorg. Chem.* **2000**, *39*, 1606−1607.

(16) Zhong, J.; Zhao, Y.; Yang, H.; Wang, J.; Liang, X.; Xiang, W. Sphere-like $CuGaS_2$ nanoparticles synthesized by a simple biomolecule-assisted solvothermal route. *Appl. Surf. Sci.* **2011**, *257*, 10188−10194.

(17) Yang, Y. Y.; Du, Y. N.; Ding, Y. S.; Zhang, S. Y.; Wang, Y. L.; Wang, L. G. Preparation and characterization of $CuGaS_2$ chalcopyrite nanoparticles via a facile solvothermal method. *Mater. Lett.* **2021**, *300*, 130150.

(18) Regulacio, M. D.; Ye, C.; Lim, S. H.; Zheng, Y.; Xu, Q. H.; Han, M. Y. Facile noninjection synthesis and photocatalytic properties of wurtzite-phase $CuGaS_2$ nanocrystals with elongated morphologies. *CrystEngComm* **2013**, *15*, 5214−5217.

(19) Zhou, Q.; Kang, S. Z.; Li, X.; Wang, L.; Qin, L.; Mu, J. One-pot hydrothermal preparation of wurtzite $CuGaS_2$ and its application as a photoluminescent probe for trace detection of l-noradrenaline. *Colloids Surf., A* **2015**, *465*, 124−129.

(20) Liu, Z.; Liu, J.; Huang, Y.; Li, J.; Yuan, Y.; Ye, H.; Zhu, D.; Wang, Z.; Tang, A. From one-dimensional to two-dimensional wurtzite $CuGaS_2$ nanocrystals: non-injection synthesis and photocatalytic evolution. *Nanoscale* **2019**, *11*, 158−169.

(21) Li, C.; Baek, J. B. Recent advances in noble metal (Pt, Ru, and Ir)-based electrocatalysts for efficient hydrogen evolution reaction. *ACS omega* **2020**, *5*, 31−40.
(22) Zhu, J.; Hu, L.; Zhao, P.; Lee, L. Y. S.; Wong, K. Y. Recent advances in electrocatalytic hydrogen evolution using nanoparticles. *Chem. Rev.* **2020**, *120*, 851−918.
(23) Wang, M.; Zhang, L.; He, Y.; Zhu, H. Recent advances in transition-metal-sulfide-based bifunctional electrocatalysts for overall water splitting. *J. Mater. Chem. A* **2021**, *9*, 5320−5363.
(24) Xu, J.; Wang, R.; Chen, X.; Zhou, R.; Zhang, J. Cu_2SnS_3 nanocrystals decorated rGO nanosheets towards efficient and stable hydrogen evolution reaction in both acid and alkaline solutions. *Mater. Today Energy* **2020**, *17*, 100435.
(25) Li, Y.; Wang, Y.; Pattengale, B.; Yin, J.; An, L.; Cheng, F.; Li, Y.; Huang, J.; Xi, P. High-index faceted $CuFeS_2$ nanosheets with enhanced behavior for boosting hydrogen evolution reaction. *Nanoscale* **2017**, *9*, 9230−9237.
(26) Maheskumar, V.; Gnanaprakasam, P.; Selvaraju, T.; Vidhya, B. Comparative studies on the electrocatalytic hydrogen evolution property of Cu_2SnS_3 and Cu_4SnS_4 ternary alloys prepared by solvothermal method. *Int. J. Hydrogen Energy* **2018**, *43*, 3967−3975.
(27) Tiwari, A. P.; Azam, A.; Novak, T. G.; Prakash, O.; Jeon, S. Chemical strain formation through anion substitution in Cu_2WS_4 for efficient electrocatalysis of water dissociation. *J. Mater. Chem. A* **2018**, *6*, 7786−7793.
(28) Kim, Y.; Tiwari, A. P.; Prakash, O.; Lee, H. Activation of ternary transition metal chalcogenide basal planes through chemical strain for the hydrogen evolution reaction. *ChemPlusChem.* **2017**, *82*, 785−791.
(29) Iwase, A.; Ng, Y. H.; Amal, R.; Kudo, A. Solar hydrogen evolution using a $CuGaS_2$ photocathode improved by incorporating reduced graphene oxide. *J. Mater. Chem. A* **2015**, *3*, 8566−8570.
(30) Gunawan, G.; Septina, W.; Ikeda, S.; Harada, T.; Minegishi, T.; Domen, K.; Matsumura, M. Platinum and indium sulfide-modified $CuInS_2$ as efficient photocathodes for photoelectrochemical water splitting. *Chem. Commun.* **2014**, *50*, 8941−8943.
(31) Kaga, H.; Tsutsui, Y.; Nagane, A.; Iwase, A.; Kudo, A. An effect of Ag (I)-substitution at Cu sites in $CuGaS_2$ on photocatalytic and photoelectrochemical properties for solar hydrogen evolution. *J. Mater. Chem. A* **2015**, *3*, 21815−21823.
(32) Kandiel, T. A.; Anjum, D. H.; Sautet, P.; Le Bahers, T.; Takanabe, K. Electronic structure and photocatalytic activity of wurtzite Cu−Ga−S nanocrystals and their Zn substitution. *J. Mater. Chem. A* **2015**, *3*, 8896−8904.
(33) Iwashina, K.; Iwase, A.; Ng, Y. H.; Amal, R.; Kudo, A. Z-schematic water splitting into H_2 and O_2 using metal sulfide as a hydrogen-evolving photocatalyst and reduced graphene oxide as a solid-state electron mediator. *J. Am. Chem. Soc.* **2015**, *137*, 604−607.
(34) Itsoponpan, T.; Thanachayanont, C.; Hasin, P. Sponge-like $CuInS_2$ microspheres on reduced graphene oxide as an electrocatalyst to construct an immobilized acetylcholinesterase electrochemical biosensor for chlorpyrifos detection in vegetables. *Sens. Actuators, B* **2021**, *337*, 129775.
(35) Luo, Z.; Jia, T.; Liu, Q.; Song, Y.; Zhou, M.; Ma, X.; Wu, J.; Qin, Z.; Wu, X. Development of $CuInS_2$/g-C_3N_4 nanolayer for efficient adsorption of elemental mercury from coal combustion flue gas. *Chem. Eng. J.* **2021**, *426*, 131905.
(36) Li, Z.; Meng, X.; Zhang, Z. Recent development on MoS_2-based photocatalysis: A review. *J. Photochem. Photobiol., C* **2018**, *35*, 39−55.
(37) Cao, Y. Roadmap and direction toward high-performance MoS_2 hydrogen evolution catalysts. *ACS Nano* **2021**, *15*, 11014−11039.
(38) Wang, Z.; Mi, B. Environmental applications of 2D molybdenum disulfide (MoS_2) nanosheets. *Environ. Sci. Technol.* **2017**, *51*, 8229−8244.
(39) Radhakrishnan, J.; Biswas, K. Facile synthesis of Ti doped MoS_2 and its superior adsorption properties. *Mater. Lett.* **2020**, *280*, 128522.
(40) Xiao, N.; Zhu, L.; Wang, K.; Dai, Q.; Wang, Y.; Li, S.; Sui, Y.; Ma, Y.; Liu, J.; Liu, B.; et al. Synthesis and high-pressure transformation of metastable wurtzite-structured $CuGaS_2$ nanocrystals. *Nanoscale* **2012**, *4*, 7443−7447.
(41) Sanikop, R.; Sudakar, C. Tailoring magnetically active defect sites in MoS_2 nanosheets for spintronics applications. *ACS Appl. Nano Mater.* **2020**, *3*, 576−587.
(42) Manickam, R.; Biswas, K. Double doping induced power factor enhancement in $CuCrO_2$ for high temperature thermoelectric application. *J. Alloys Compd.* **2019**, *775*, 1052−1056.
(43) You, Y.; Ye, Y.; Wei, M.; Sun, W.; Tang, Q.; Zhang, J.; Chen, X.; Li, H.; Xu, J. Three-dimensional MoS_2/rGO foams as efficient sulfur hosts for high-performance lithium-sulfur batteries. *Chem. Eng. J.* **2019**, *355*, 671−678.
(44) Zhang, X.; Guo, Y.; Tian, J.; Sun, B.; Liang, Z.; Xu, X.; Cui, H. Controllable growth of MoS_2 nanosheets on novel Cu_2S snowflakes with high photocatalytic activity. *Appl. Catal., B* **2018**, *232*, 355−364.
(45) Wang, X.; Wang, J.; Zhang, X.; Tian, Q.; Liu, M.; Cai, N.; Xue, Y.; Chen, W.; Li, W.; Yu, F. Nitrogen-Doped Cu_2S/MoS_2 Heterojunction Nanorod Arrays on Copper Foam for Efficient Hydrogen Evolution Reaction. *ChemCatChem.* **2019**, *11*, 1354−1361.
(46) Gao, B.; Du, X.; Ma, Y.; Li, Y.; Li, Y.; Ding, S.; Song, Z.; Xiao, C. 3D flower-like defected MoS_2 magnetron-sputtered on candle soot for enhanced hydrogen evolution reaction. *Appl. Catal., B* **2020**, *263*, 117750.
(47) Shinagawa, T.; Garcia-Esparza, A. T.; Takanabe, K. Insight on Tafel slopes from a microkinetic analysis of aqueous electrocatalysis for energy conversion. *Sci. Rep.* **2015**, *5*, 13801.
(48) He, Q.; Huang, S.; Liu, M.; Li, P.; Sun, W.; Hou, L. Synthesis of CoS_2/SnO_2@MoS_2 nanocube heterostructures for achieving enhanced electrocatalytic hydrogen evolution in acidic media. *Inorg. Chem. Front.* **2020**, *7*, 2660−2668.
(49) Zhou, Z.; Wei, L.; Wang, Y.; Karahan, H. E.; Chen, Z.; Lei, Y.; Chen, X.; Zhai, S.; Liao, X.; Chen, Y. Hydrogen evolution reaction activity of nickel phosphide is highly sensitive to electrolyte pH. *J. Mater. Chem. A* **2017**, *5*, 20390−20397.
(50) An, L.; Feng, J.; Zhang, Y.; Wang, R.; Liu, H.; Wang, G. C.; Cheng, F.; Xi, P. Epitaxial heterogeneous interfaces on N-$NiMoO_4$/NiS_2 nanowires/nanosheets to boost hydrogen and oxygen production for overall water splitting. *Adv. Funct. Mater.* **2019**, *29*, 1805298.
(51) Anantharaj, S.; Kundu, S. Do the evaluation parameters reflect intrinsic activity of electrocatalysts in electrochemical water splitting? *ACS Energy Lett.* **2019**, *4*, 1260−1264.
(52) Deng, Y.; Liu, Z.; Wang, A.; Sun, D.; Chen, Y.; Yang, L.; Pang, J.; Li, H.; Li, H.; Liu, H.; Zhou, W. Oxygen-incorporated MoX (X: S, Se or P) nanosheets via universal and controlled electrochemical anodic activation for enhanced hydrogen evolution activity. *Nano Energy* **2019**, *62*, 338−347.
(53) Jin, J.; Yin, J.; Liu, H.; Huang, B.; Hu, Y.; Zhang, H.; Sun, M.; Peng, Y.; Xi, P.; Yan, C. H. Atomic sulfur filling oxygen vacancies optimizes H absorption and boosts the hydrogen evolution reaction in alkaline media. *Angew. Chem.* **2021**, *133*, 14236−14242.
(54) Harvey, A.; Backes, C.; Gholamvand, Z.; Hanlon, D.; McAteer, D.; Nerl, H. C.; McGuire, E.; Seral-Ascaso, A.; Ramasse, Q. M.; McEvoy, N.; et al. Preparation of gallium sulfide nanosheets by liquid exfoliation and their application as hydrogen evolution catalysts. *Chem. Mater.* **2015**, *27*, 3483−3493.
(55) Basu, M.; Nazir, R.; Fageria, P.; Pande, S. Construction of CuS/Au heterostructure through a simple photoreduction route for enhanced electrochemical hydrogen evolution and photocatalysis. *Sci. Rep.* **2016**, *6*, 34738.
(56) Kush, P.; Deori, K.; Kumar, A.; Deka, S. Efficient hydrogen/oxygen evolution and photocatalytic dye degradation and reduction of aqueous Cr (VI) by surfactant free hydrophilic Cu_2ZnSnS_4 nanoparticles. *J. Mater. Chem. A* **2015**, *3*, 8098−8106.
(57) Asiri, A. M.; Adeosun, W. A.; Khan, S. B.; Alamry, K. A.; Marwani, H. M.; Zakeeruddin, S. M.; Graeetzel, M. $NiCuCoS_3$ chalcogenide as an efficient electrocatalyst for hydrogen and oxygen evolution. *J. Mater. Res. Technol.* **2021**, *15*, 4826−4837.

https://doi.org/10.1021/acsomega.2c05116
ACS Omega 2022, 7, 43883−43893

(58) Chua, X. J.; Luxa, J.; Eng, A. Y. S.; Tan, S. M.; Sofer, Z.; Pumera, M. Negative electrocatalytic effects of p-doping niobium and tantalum on MoS_2 and WS_2 for the hydrogen evolution reaction and oxygen reduction reaction. *ACS Catal.* **2016**, *6*, 5724−5734.
(59) Radhakrishnan, J.; Kareem, A.; Senthilkumar, S.; Biswas, K. Facile synthesis of S-vacancy induced electrochemical HER activity in Multilayered Sn doped MoS_2. *J. Alloys Compd.* **2022**, *917*, 165444.
(60) Lai, B.; Singh, S. C.; Bindra, J. K.; Saraj, C. S.; Shukla, A.; Yadav, T. P.; Wu, W.; McGill, S. A.; Dalal, N. S.; Srivastava, A.; Guo, C. Hydrogen evolution reaction from bare and surface-functionalized few-layered MoS_2 nanosheets in acidic and alkaline electrolytes. *Mater. Today Chem.* **2019**, *14*, 100207.
(61) Huang, Q.; Liu, M.; Chen, J.; Wan, Q.; Tian, J.; Huang, L.; Jiang, R.; Wen, Y.; Zhang, X.; Wei, Y. Facile preparation of MoS_2 based polymer composites via mussel inspired chemistry and their high efficiency for removal of organic dyes. *Appl. Surf. Sci.* **2017**, *419*, 35−44.
(62) Han, S.; Liu, K.; Hu, L.; Teng, F.; Yu, P.; Zhu, Y. Superior adsorption and regenerable dye adsorbent based on flower-like molybdenum disulfide nanostructure. *Sci. Rep.* **2017**, *7*, 43599.
(63) Wang, S.; Yang, B.; Liu, Y. Synthesis of a hierarchical SnS_2 nanostructure for efficient adsorption of Rhodamine B dye. *J. Colloid Interface Sci.* **2017**, *507*, 225−233.
(64) Wang, C.; Shi, W.; Zhu, K.; Luan, X.; Yang, P. Chemical Vapor Deposition Growth of MoS_2 on g-C_3N_4 Nanosheets for Efficient Removal of Tetracycline Hydrochloride. *Langmuir* **2022**, *38*, 5934−5942.

https://doi.org/10.1021/acsomega.2c05116
ACS Omega 2022, 7, 43883−43893